ORNL/TM-2016/371

Toughness and High-Temperature Steam Oxidation Evaluations of Advanced Alloys for Core Internals

Lizhen Tan
Bruce A. Pint
Xiang Chen

September 16, 2016

OAK RIDGE NATIONAL LABORATORY
MANAGED BY UT-BATTELLE FOR THE US DEPARTMENT OF ENERGY

ORNL/TM-2016/371

Light Water Reactor Sustainability (LWRS) Program

TOUGHNESS AND HIGH-TEMPERATURE STEM OXIDATION EVALUATIONS OF ADVANCED ALLOYS FOR CORE INTERNALS

Lizhen Tan, Bruce A. Pint, Xiang Chen

Date Published: September 16, 2016

Prepared by
OAK RIDGE NATIONAL LABORATORY
Oak Ridge, Tennessee 37831-6283
managed by
UT-BATTELLE, LLC
for the
US DEPARTMENT OF ENERGY
under contract DE-AC05-00OR22725

CONTENTS

Page

LIST OF FIGURES

Figure **Page**

LIST OF TABLES

Table **Page**

ACKNOWLEDGMENTS

This research was sponsored by the U.S. Department of Energy (DOE), Office of Nuclear Energy (NE), for the Light Water Reactor Sustainability (LWRS) Program Research and Development (R&D) effort. We gratefully acknowledge the support provided by Richard A. Reister of DOE-NE, Federal Project Director of Light Water Reactor Deployment; Kathryn A. McCarthy of Idaho National Laboratory (INL), Director of the LWRS Program Technical Integration Office (TIO); Donald L. Williams, Jr. of Oak Ridge National Laboratory (ORNL), Deputy Director of the LWRS Program TIO; Cathy J. Barnard of INL, Program Manager of the LWRS Program TIO; and Keith J. Leonard of ORNL, Lead of Materials Aging and Degradation R&D Pathway of the LWRS Program.

The authors are grateful to Raj Pathania (Electric Power Research Institute [EPRI]) and Larry Nelson (JLN Consulting) for their managing and coordinating the Advanced Radiation Resistant Materials (ARRM) program; Martin Morra (General Electric [GE] Global Research Center), David Sandusky (retiree of GE Nuclear Energy), and Benjamin Sutton (EPRI) for helpful discussions and sharing the alloys; David Hoelzer of ORNL for providing the 14YWT oxide-dispersion-strengthened alloy and helpful discussions, and Eric Manneschmidt, George Garner, and Tracie Lowe of ORNL for testing and preparing the samples. Maxim Gussev of ORNL is also appreciated for reviewing this report.

EXECUTIVE SUMMARY

Life extension of the existing nuclear reactors imposes irradiation of high fluences to structural materials, resulting in significant challenges to the traditional reactor materials such as type 304 and 316 stainless steels. Advanced alloys with superior radiation resistance will increase safety margins, design flexibility, and economics for not only the life extension of the existing fleet but also new builds with advanced reactor designs. The Electric Power Research Institute (EPRI) teamed up with Department of Energy (DOE) to initiate the Advanced Radiation Resistant Materials (ARRM) program, aiming to develop and test degradation resistant alloys from current commercial alloy specifications by 2021 to a new advanced alloy with superior degradation resistance in light water reactor (LWR)-relevant environments by 2024.

A total of fifteen commercial and advanced alloys, including three variants of Alloy 625, have been down-selected for investigation under the ARRM program. Thirteen of the alloys, together with 316L and T91 as the reference steels, have been procured. It includes a total of one zirconium alloy (Zr–2.5Nb), four ferritic steels (T91, Grade 92, Alloy 439, and 14YWT), three austenitic stainless steels (316L, 310, and 800), and eight Ni-based superalloys (625, 625DA, 625-plus, 690, 725, X750, and C22). The procurement of the other down-selected alloys such as 718 and Grade 26 Ti-alloy is in progress. With careful microstructural examinations conducted at GE Global Research Center and Oak Ridge National Laboratory, it has been confirmed that most of the procured alloys have acceptable microstructures for tests under the ARRM program. However, the as-procured Alloy 439 does not have an acceptable microstructure because of the coarse grains and the presence of many intragranular cracks.

A thermomechanical treatment (TMT) was successfully developed on the as-procured Alloy 439, achieving significantly refined grains. To have acceptable "flawless" microstructure for mechanical property and ion irradiation resistance screening, ultrasonic non-destructive examination technique was used to guide specimen extraction. A new heat of Alloy 439 with a well-controlled microstructure (with fine grains and free of cracks) will be procured if the screening tests yield promising results.

The fine-grained Alloy 439 after the TMT exhibited some increases in both strength and ductility tested using type SS-3 specimens, as well as improvements in impact toughness tested using half-size Charpy V-notch specimens, compared to the as-procured coarse-grained Alloy 439. Oxide-dispersion-strengthened alloy 14YWT showed significantly greater strength than Grade 92 and Alloy 439, with ductility comparable to Grade 92 but less than Alloy 439. Alloy 439 exhibited the highest upper-shelf energy (USE) of ~57 J with a mathematical ductile-brittle transition temperature (DBTT) of 16.0°C at 1/2USE, which are higher than Grade 92 with an USE of ~27 J and a DBTT of −19.7°C. The super-high strength of 14YWT led to a low USE of ~5 J with a low DBTT of −79.8°C. Fracture toughness tests of 14YWT in the ductile regime using 0.2T compact tension specimens indicated a quick decrease in fracture toughness from ~160 MPa√m at room temperature to ≤69 MPa√m at temperatures above 200°C, accompanied by a quick increase in tearing modulus from ~6.6±2.1 at 25–600°C to 36.5 at 700°C.

Steam oxidation tests at 1 atmosphere with ~10 ppb oxygen at 600 and 650°C were conducted on the procured alloy coupons, which were weighed at 500-h intervals with a targeted exposure time of 5000 h. Alloy Zr–2.5Nb was only tested one cycle (500 h) at 600 and 650°C because of the exceptional weight gains and extensive oxide scales formed on the coupons. Ferric steels Grade 92, Alloy 439, and 14YWT showed moderate weight gains in a descending order, which are believed to be primarily determined by the chromium content (9, 18, and 14Cr, respectively) and grain size (~40, ~50, and ~0.8 μm, respectively) in the steels. Oxide scale characterization by optical microscopy revealed approximate consistency between the scale thickness and weight gains of Grade 92 and 14YWT, but not Alloy 439. Detailed

analysis will be conducted to elucidate the discrepancy. Austenitic stainless steel 316L exhibited significant weight losses with extensive scale exfoliation. The significantly increased amounts of chromium and nickel in Alloy 800 and the Ni-based superalloys led to small or negligible weight changes. Detailed ranking regarding the steam oxidation resistance of the alloy will be deduced when all the alloy coupons accomplish 5000 h exposures at 600 and 650°C in next fiscal year.

In summary, Alloy X-750 was procured from Carpenter Technology and Bodycote in this year. An appropriate TMT was developed on Alloy 439 to obtain materials with refined grain size for property screening tests. Charpy V-notch impact tests were completed for the three ferritic steels Grade 92, Alloy 439, and 14YWT. Fracture toughness tests at elevated temperatures were completed for 14YWT. The tests will be completed for the other alloys in next fiscal year. Steam oxidation tests of the three ferritic steels, 316L, and Zr–2.5Nb have been completed. The steam tests of the Ni-based superalloys and the other austenitic stainless steels will be continued and finished in next fiscal year. Performance ranking in terms of steam oxidation resistance and impact/fracture toughness of the alloys will be deduced.

1. INTRODUCTION

Nuclear power currently provides a significant fraction of the United States' non-carbon emitting power generation. In future years, nuclear power must continue to generate a significant portion of the nation's electricity to meet the growing electricity demand, clean energy goals, and to ensure energy independence. New reactors will be an essential part of the expansion of nuclear power. However, given limits on new builds imposed by economics and industrial capacity, the extended service of the existing fleets will also be required.

Nuclear reactors present a very harsh environment for components service. Components within a reactor core must tolerate high temperatures, water, stress, vibration, and an intense neutron field. With the nominal irradiation temperature of ~290°C in light water reactors (LWRs), actual component temperatures range from 270°C to 370°C depending on the relative position of the component within the reactor core and relative amounts of cooling and gamma heating. Degradation of materials in this environment can lead to reduced performance, and in some cases, sudden failure.

Extending the service life of a reactor will increase the total neutron fluence to each component and may result in radiation-induced effects not yet observed in LWR conditions, although this form of degradation has been observed in fast reactor conditions. Radiation-induced processes must be carefully considered for higher fluences, particularly the influence of radiation-induced segregation (RIS), swelling, and/or precipitation on embrittlement. Neutron irradiation field can produce large property and dimensional changes in materials. For LWRs, high-temperature embrittlement and creep are not common problems due to the lower reactor temperature. However, radiation embrittlement, phase transformation, segregation, and swelling have all been observed in reactor components. Increases in neutron fluence may exacerbate radiation-induced or -enhanced microstructural and property changes. Comprehensive reviews on radiation effects on the traditional structural materials of LWRs can be found in Ref. [1,2,3].

It is desirable to have advanced alloys that possess greater radiation resistance than the traditional reactor materials. The use of such advanced alloys in replacing the traditional reactor materials for the extension of the existing fleets and the building of new reactors will bring improved safety margins and economics. To identify and develop advanced radiation resistant materials, Electric Power Research Institute (EPRI) has partnered with Department of Energy (DOE) Light Water Reactor Sustainability Program to conduct an Advanced Radiation Resistant Materials (ARRM) program. The EPRI report of "Critical Issues Report and Roadmap for the Advanced Radiation-Resistant Materials Program" [4] reviewed the current commercial and advanced alloys that are applicable as core structural materials of LWRs and laid out a detailed research plan to meet the goal of the program.

Procurement of high quality alloys of the candidate materials, selected for testing under the ARRM program, has been mostly completed. Table 1 lists the procured alloys with nominal compositions in weight percentages and heat numbers. Four of the alloys, i.e., 718, Grade 26 Ti-alloy, 12Cr ferritic-martensitic steel, and high Cr and Al oxide-dispersion-strengthened alloy, have not been procured. The materials having acceptable chemistry homogeneity and microstructural uniformity were used for testing under the ARRM program. Non-irradiated materials testing and proton irradiation testing have been pursued following relevant ASTM standards. This report presents the testing results of toughness and high-temperature steam oxidation of the procured alloys.

Table 1. Identified commercial, advanced, and reference alloys to be tested in the ARRM program

Commercial Alloy		Nominal composition	Heat number
Ni-base	625	61Ni–22Cr–9Mo–4Nb4Fe	602051
	625 direct age		JG81
	625-plus	625+Ti	215846
	690	60Ni–30Cr–10Fe	NX7075HK11
	725	58Ni–22Cr–8Mo–8Fe–4NbTi	416408
	X-750	71Ni–16Cr–8Fe–2.6TiNbAl	418365
	C22	58Ni–22Cr–14Mo–3W3Fe	416270
	718*	53Ni–20Cr–17Fe–5.2Nb–3MoTiAl	
Austenitic	800	Fe–20Cr–32Ni–TiAl	07032
	310	Fe–25Cr–20Ni	011511
Others	Zr–2.5Nb		251602
	Ti-alloys*	Grade 26 with 0.1 Ru	
Advanced alloy			
9Cr FM[1]	Grade 92	Fe–9Cr–2WVNb	011448
12Cr FM	To be determined, e.g., HT9		
High-Cr (>14Cr) ferritic	439	Fe–18Cr	011438
9-14Cr ODS[2]	14YWT	Fe–14Cr–3W–TiYO	FCRD-NFA1
High-Cr&Al ODS	To be determined		
Reference Alloy			
Austenitic	316L	Fe–16Cr–10Ni–2Mo	857115
FM	T91	Fe–9Cr–1MoVNbN	F318051

[1] FM: ferritic-martensitic
[2] ODS: oxide-dispersion-strengthened
* Procurement in progress

1.1 Reprocessing of Alloy 439

The microstructure of all the procured alloys was examined in terms of grain size and the amount of inclusions or defects. It was found that most of the alloys have satisfactory microstructures after removing about 5-20 mm surface materials. However, the microstructure of the as-procured Alloy 439 is not acceptable for tests under the ARRM program because of the coarse grains and many intragranular cracks close to the center of the forged plates as shown in Figure 1.

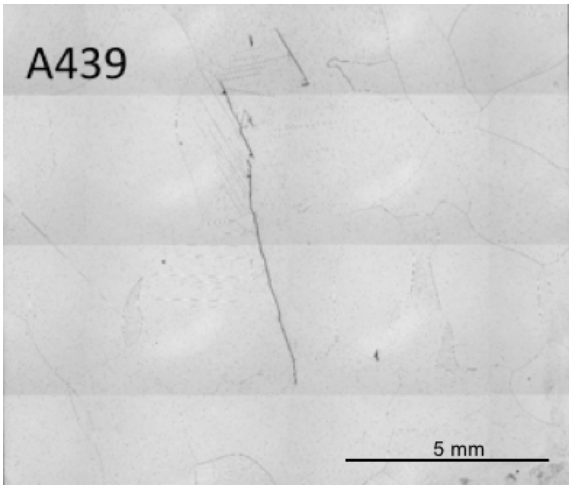

Figure 1. Optical micrograph showing cracks in the as-procured Alloy 439.

To have some acceptable material for screening the mechanical properties and ion irradiation resistance of this alloy, thermomechanical treatments (TMTs) were explored to obtain refined grains. Warm-rolling with 60% thickness reduction at 300°C followed by annealing at 950°C for 10 min and air cooling achieved refined grains in the Alloy 439 after two types of TMT practices. Figure 2 shows optical micrographs of the reprocessed Alloy 439 compared to the as-procured Alloy 439, which indicates that the TMT refined the grain size to ~50 µm from the as-procured grain size of ~2 mm. Reprocessing is not able to get rid of the pre-existing cracks. A partial vertical crack is seeable at the bottom of Figure 2b.

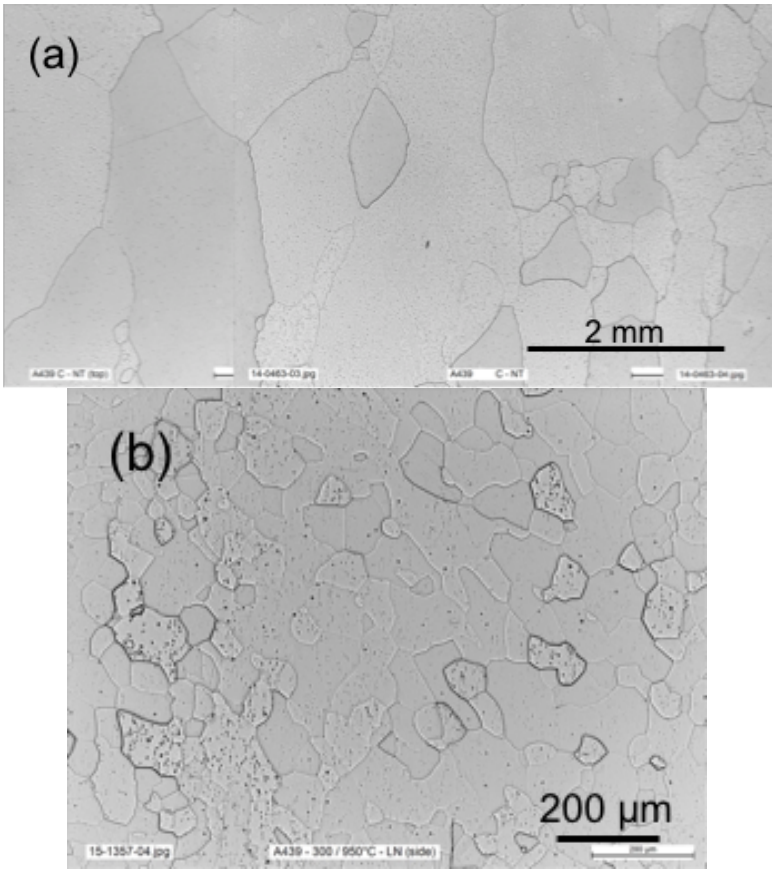

Figure 2. Optical micrographs showing distinct grain sizes in the (a) as-procured and (b) reprocessed Alloy 439.

Ultrasonic non-destructive examination (NDE) was performed on the reprocessed pieces of Alloy 439 to locate "flawless" material for specimen extraction. An example of a piece of reprocessed Alloy 439 is shown in Figure 3a, with the upper left corner cut for metallographic study as shown in Figure 2a. The ultrasonic NDE result of this piece is shown in Figure 3b, showing the flaws in bright. A large amount of flaws is primarily at the left side with some small defects at upper left side of this piece. Metallographic study indicated that the large area of bright feature is resulted from many large cracks approximately parallel to the surface of this piece. Different types of specimens, such as type SS-3 tensile, half-size Charpy impact, 0.2T compact tension (solid black lines), and coupon for steam oxidation, are marked on the ultrasonic NDE result to guide the sample extraction. Similar ultrasonic NDE was conducted on other reprocessed pieces to guide sample extraction for ion irradiation study. A new heat of Alloy 439 with a well-controlled microstructure (with fine grains and free of cracks) will be procured if the screening tests yield promising results.

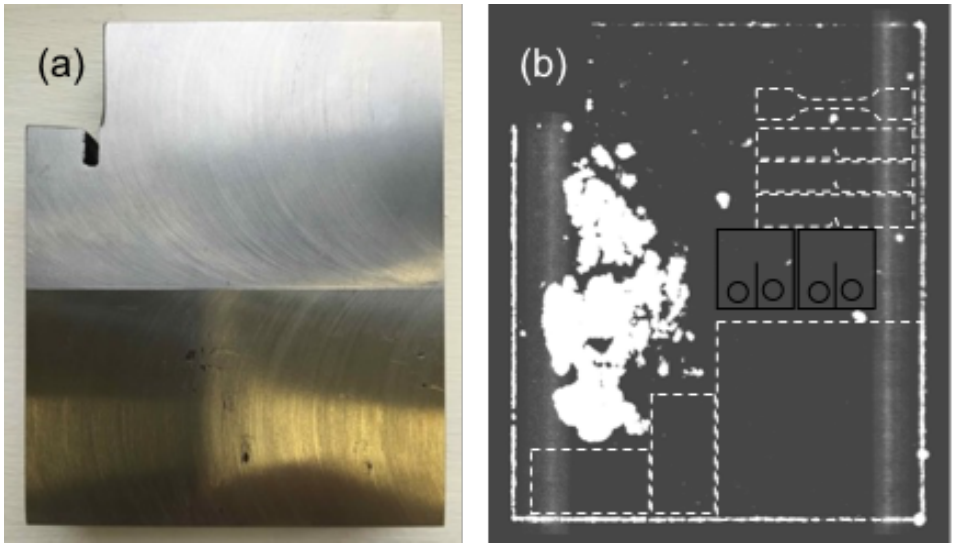

Figure 3. (a) A piece of reprocessed Alloy 439 after fly-cut for (b) ultrasonic NDE.

Tensile tests using type SS-3 specimens with a size of 0.06”×0.03”×0.3” for the gauge section were conducted on both the coarse-grained (CG) and fine-grained (FG) Alloy 439 from room temperature to 600°C. The tensile properties, including yield strength (YS), tensile strength (TS), uniform elongation (UE), and total elongation (TE), are plotted in Figure 4. The FG microstructure yielded slightly higher YS and TS, together with slightly improved UE and TE, compared to the CG microstructure.

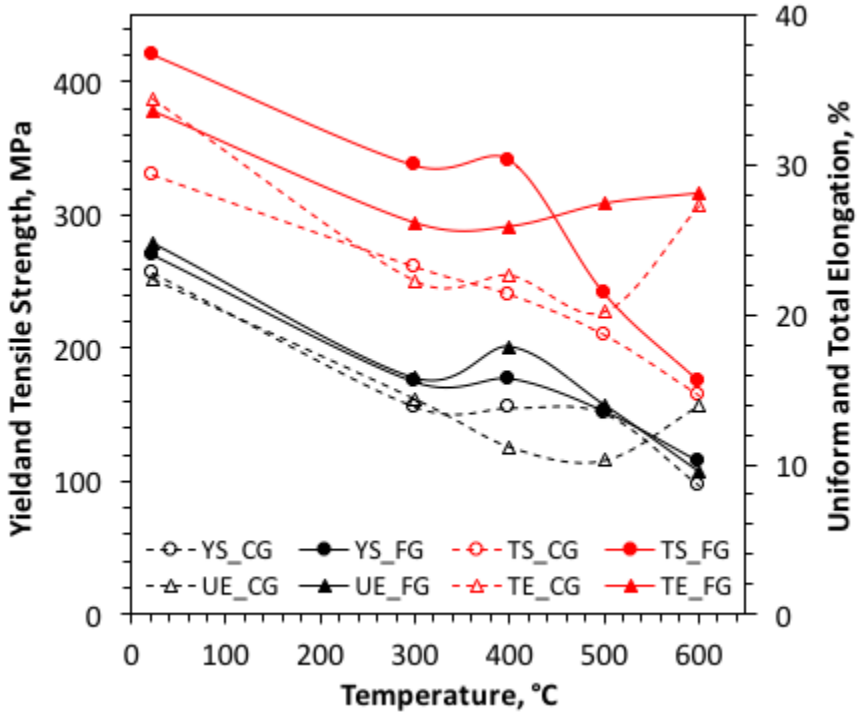

Figure 4. Tensile properties of the coarse-grained (CG) and fine-grained (FG) Alloy 439.

Figure 5 compares the tensile properties of the fine-grained Alloy 439 to the results of Grade 92 and 14YWT collected in last fiscal year [5]. Alloy 439 has the lowest strength with the smallest decreases with increasing temperature. In contrast, 14YWT has the highest strength with the greatest decreases with increasing temperature. Alloy 439 has the highest ductility. Despite the highest strength of 14YWT, its ductility is comparable to Grade 92, with even slightly better uniform elongations than Grade 92.

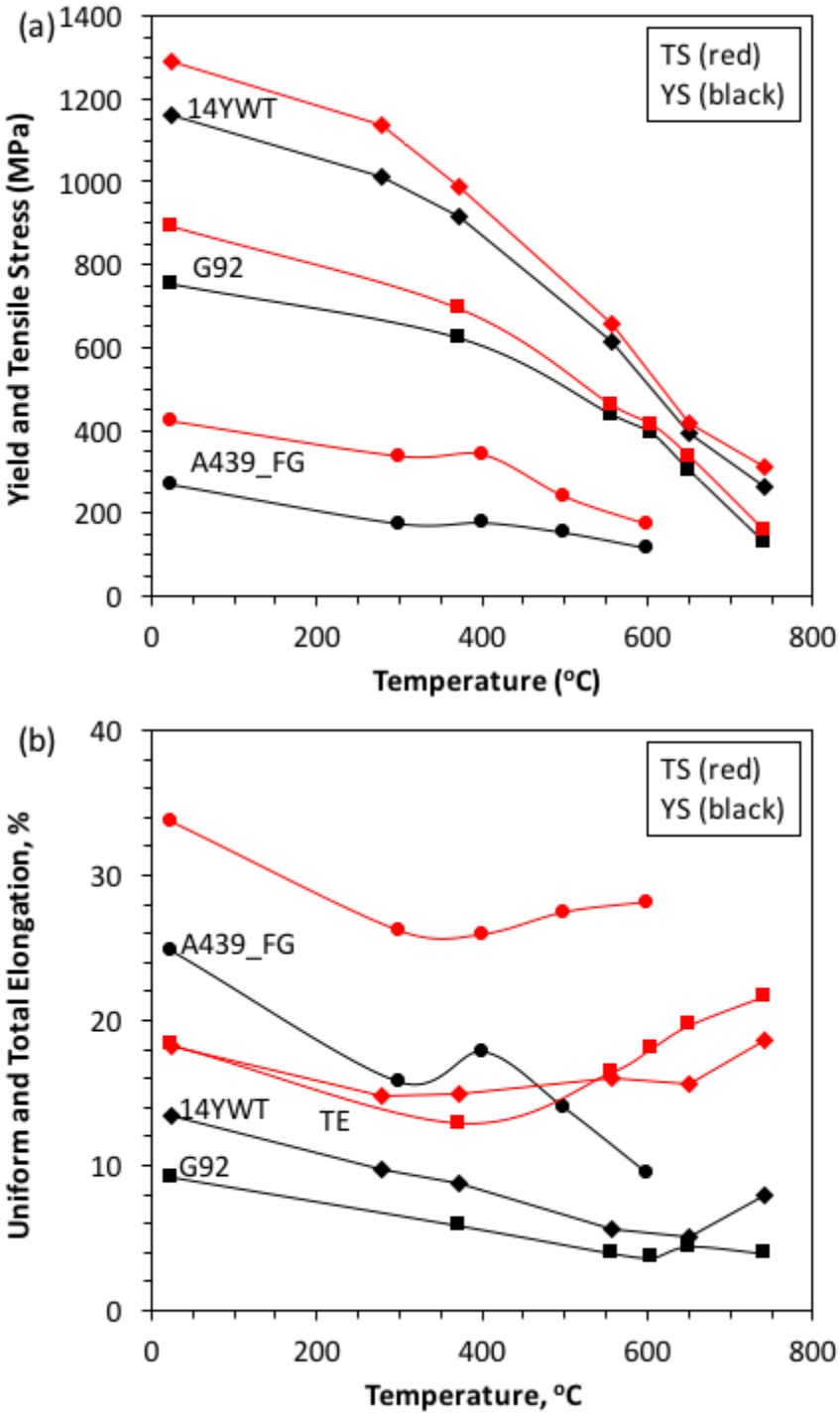

Figure 5. (a) Yield and tensile strength and (b) uniform and total elongation comparison of Grade 92, fine-grained Alloy 439, and 14YWT.

2. IMPACT AND FRACTURE TOUGHNESS

2.1 Charpy Impact Toughness

Charpy impact resistance is an important property of ferritic steels, which influences the application condition of the materials. Charpy impact tests of the reprocessed Alloy 439 were conducted on a Tinius Olsen Charpy 300 ft-lb machine according to the ASTM standard E23-12c, "Standard test methods for notched bar impact testing of metallic materials." The measurement calibration of the Charpy machine is performed annually through testing of specimens with certified values to verify the accuracy of the machine. The certified specimens are obtained from the National Institute of Standards and Technology (NIST). Half-size Charpy V-notch specimens with a specification shown in Figure 6 were used to screen the absorbed impact energies at temperatures ranging from –150°C to 300°C to determine ductile-brittle transition temperature (DBTT) and upper-shelf energy (USE). The specimens were machined in the T-L (transverse-longitudinal) orientation with V-notch aligned with the longitudinal direction of the plate because of the generally worst impact resistance in this orientation compared to other orientations.

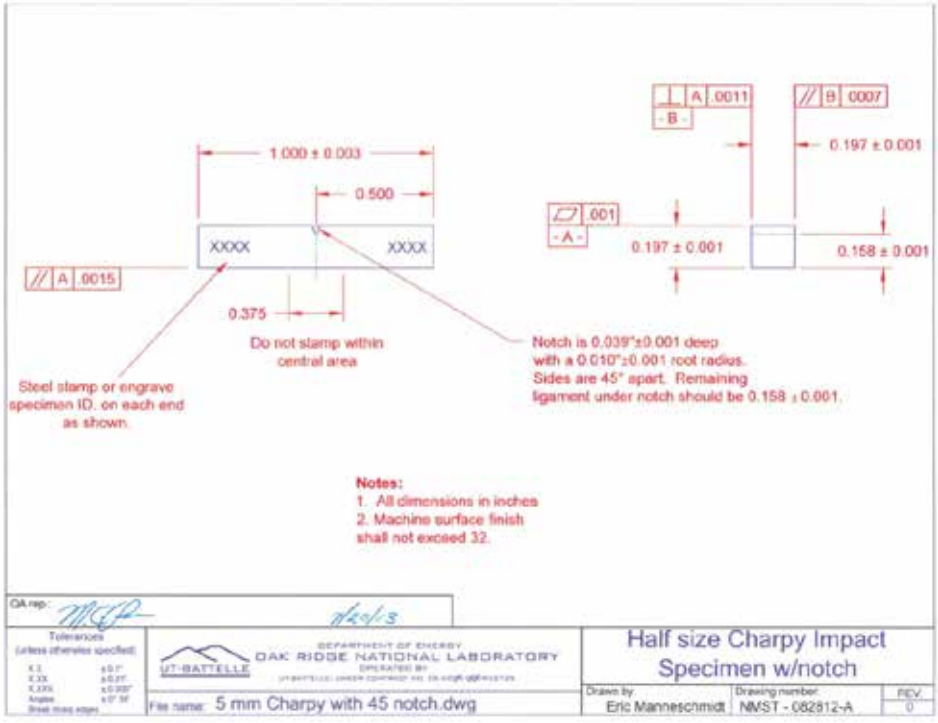

Figure 6. Specification of half-size Charpy V-notch impact specimen.

The test results of the reprocessed Alloy 439 specimens are plotted in Figure 7. Charpy impact test results of the as-procured Alloy 439, Grade 92, and 14YWT obtained in last fiscal year are included for comparison. To obtain DBTT and USE, an impact energy-temperature curve was generated by fitting the data with a hyperbolic tangent function $E = a + b \tanh[(T - T_0)/c]$, where T is test temperature and a, b, c and T_0 are regression coefficients. In this study, T_0 is the mathematical DBTT, corresponding to the mean value of USE and lower-shelf energy (LSE), i.e., 1/2USE assuming LSE = 0 in this study. Results of the as-received coarse-grained (CG) Alloy 439 are included in Figure 7a for comparison. The refined-grains (FG) increased USE and decreased DBTT (T_0). Figure 7b shows the Charpy impact test results of Alloy 439 with refined-grains, compared to Grade 92 and 14YWT. The USE of Alloy 439 (~57 J) is about two times of Grade 92 (~27 J) and ~11 times of 14YWT (~5 J). Specimens of Grade 92 in the L-T orientations

showed higher an USE and lower DBTT (T_0), which is consistent with general observations on specimen orientation dependence. Comparing DBTT (T_0), Alloy 439 (16.0°C) is higher than Grade 92 (–19.7°C) and 14YWT (–79.8°C). However, engineering DBTT is determined at 6.5 J for the half-size specimen (5 × 5 × 25 mm), lower than the 41 J for full-size specimen (10 × 10 × 55 mm) [6]. The low USE of 14YWT (~5J) suggests that special engineering designs are needed for applications of 14YWT.

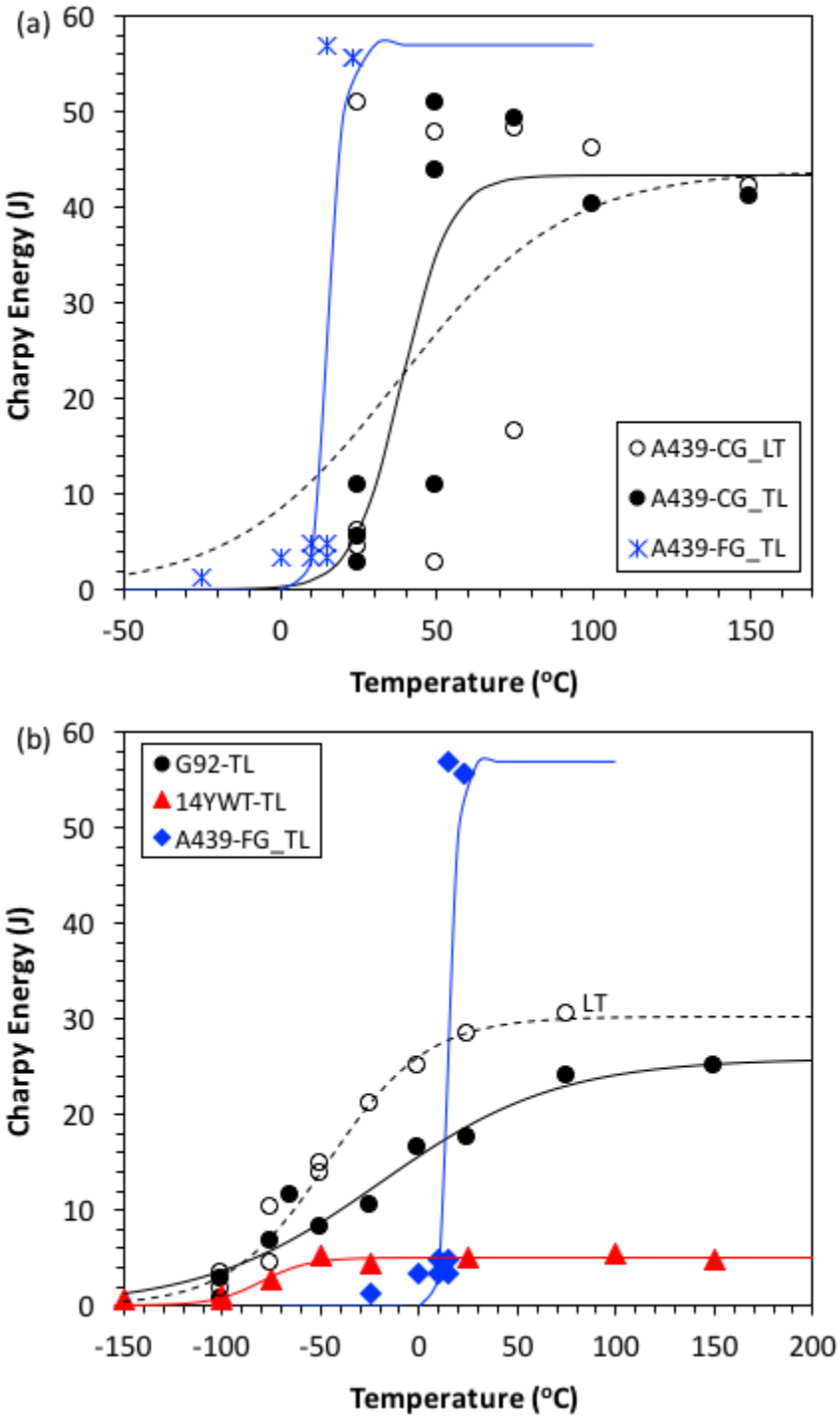

Figure 7. Charpy impact test results of fine-grained Alloy 439 compared to (a) coarse-grained Alloy 439 and (b) Grade 92 and 14YWT.

2.2 Fracture Toughness of 14YWT in the ductile regime

Compact tension (0.2T) specimens according to the specification in Figure 8 were extracted from the procured plates of 14YWT along the T-L orientation (i.e., extrusion direction). A total of eight specimens, with one specimen per plate thickness (0.35”), were extracted from ½-thickness of the 14WYT plate. Fracture toughness tests were conducted with a computer-controlled test and data acquisition system in accordance with the ASTM Standard E1820, “Standard Test Method for Measurement of Fracture Toughness” for the ductile regime at elevated temperatures (25–700°C). The specimens were fatigue pre-cracked to a ratio of the crack length to specimen width (a/W) of about 0.5 before fracture testing. Specimens were tested in the laboratory on a 98-kN (22-kip) capacity servo-hydraulic machine. All tests were conducted in strain control, with an outboard clip gage having a central flexural beam that was instrumented with four strain gages in a full-bridge configuration.

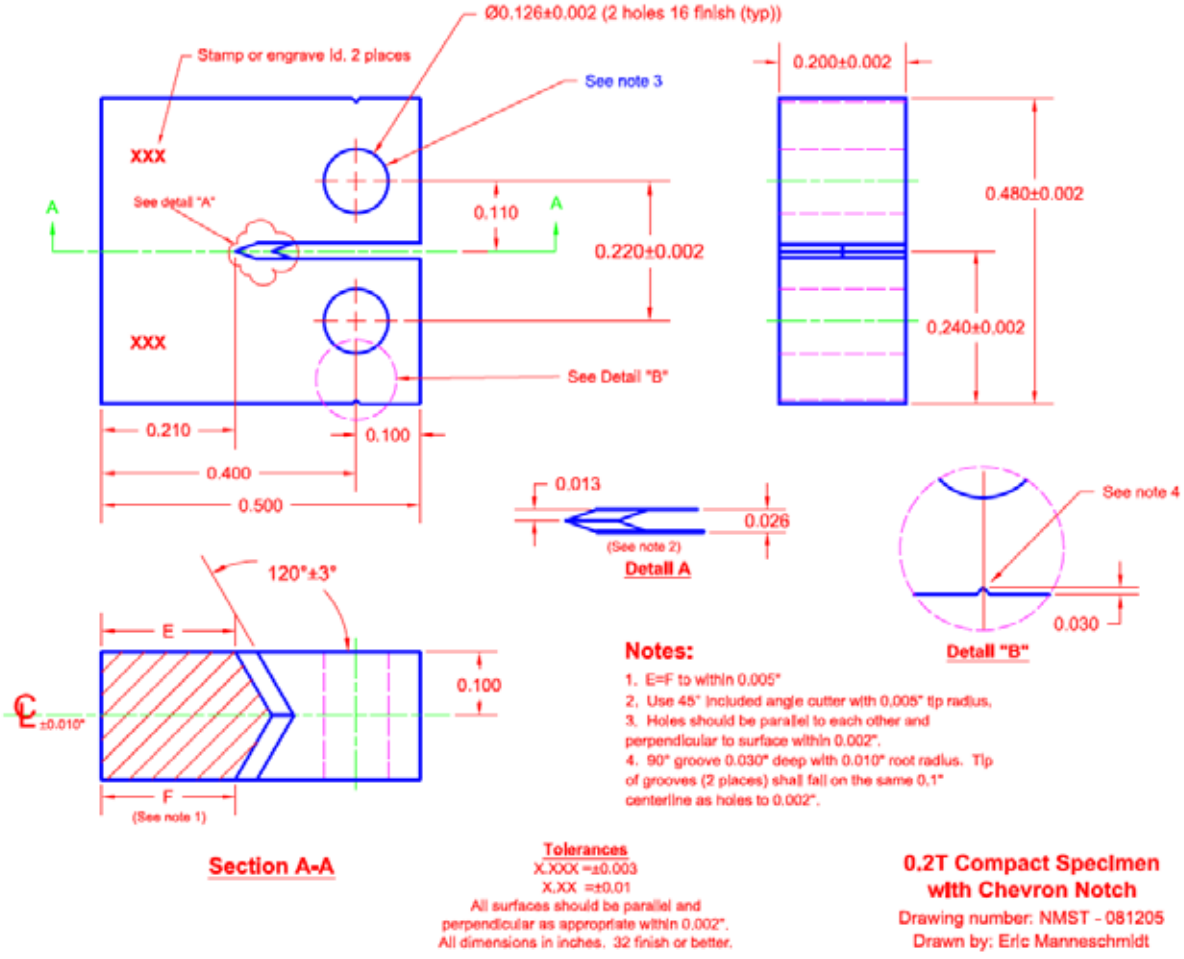

Figure 8. Specification of 0.2T compact specimen for fracture toughness test.

Figure 9 shows the photos of the broken specimens with the left- and right-half specimen showing the side-view and fractured surface, respectively, of each specimen. The broken specimens were examined with a calibrated measuring optical microscope to determine the initial and final crack lengths.

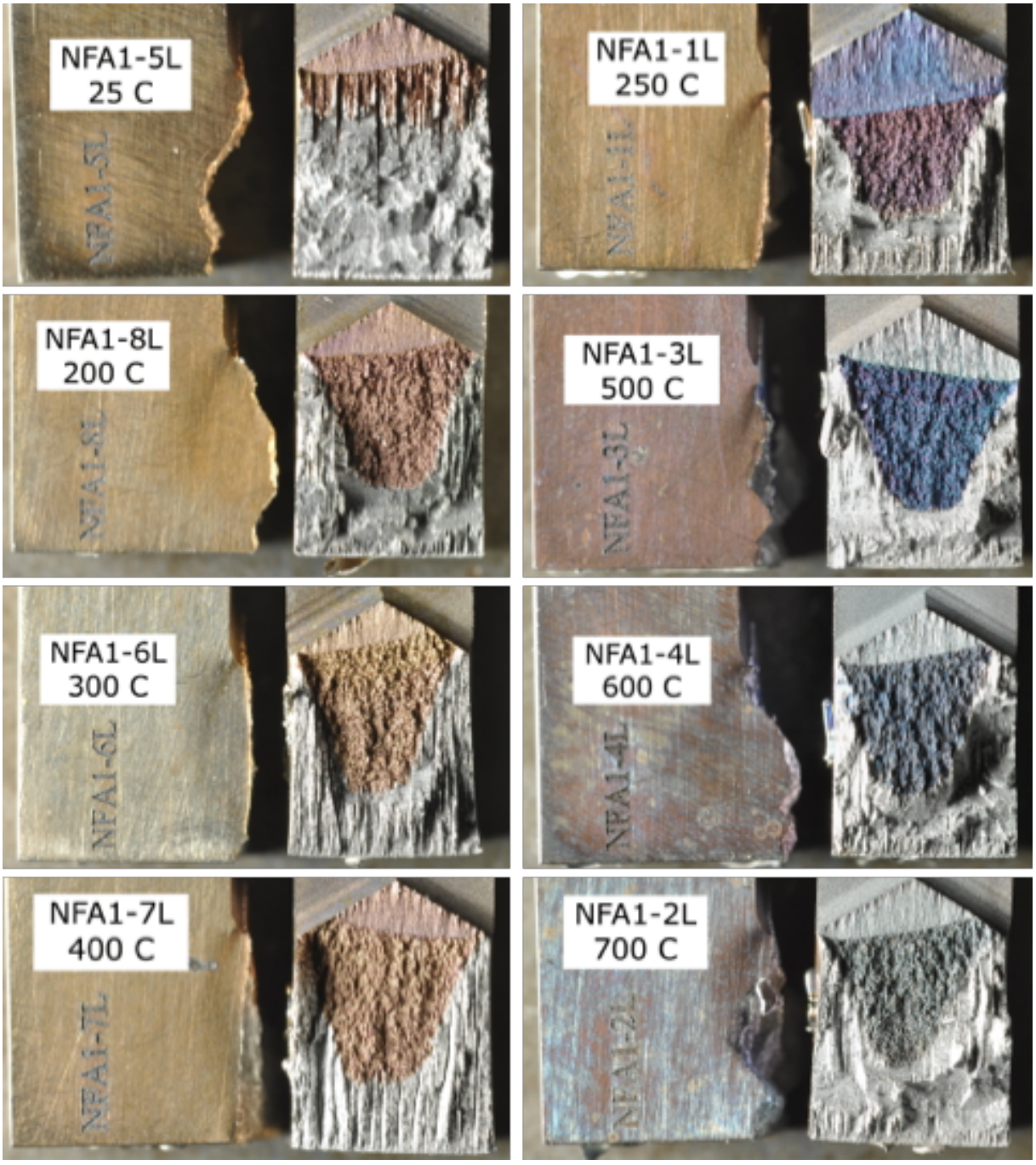

Figure 9. Photos of the tested 0.2T compact specimens of 14YWT (heat FCRD-NFA1) at 25 to 700°C.

J-R curves of the fracture toughness tests in the ductile regime at 25 to 700°C are shown in Figure 10. Values of *J*-integral at the onset of stable crack growth, J_Q, were converted to their equivalent values in terms of stress intensity K_{JQ} by the equation of $K_{JQ} = \sqrt{J_Q \frac{E}{1-\nu^2}}$, where E is Young's modulus and ν is Poisson ratio (= 0.28). In the meantime, tearing modulus (unitless) was also estimated from the slopes of J-R curves times $E/[(\sigma_{YS} + \sigma_{TS})/2]^2$ with σ_{YS} and σ_{TS} as the yield and tensile strength of the material at each test temperature. The test results of K_{JQ} and tearing modulus for 14YWT at 25–700°C are shown in

Figure 11 with filled symbols and solid trend lines. The K_{JQ} results of a different heat (SM10) of 14YWT are included in Figure 11a for comparison, which were tested using sub-size disc compact tension specimens with the nominal dimensions of 12.5 mm in diameter and 3 mm in thickness and with a 6.35 mm long wire-cut notch in L–T orientation [7]. The SM10 heat exhibited a fracture toughness transition from ~144 MPa√m to ≤82 MPa√m after 200°C. In contrast, the FCRD-NFA1 heat from this work showed a quick decrease in fracture toughness to ≤69 MPa√m at 200°C. Other than room temperature, the FCRD-NFA1 heat had slightly lower fracture toughness than the SM10 heat, which may be primarily attributable to the differences in specimen orientations (T–L in this work versus L–T of the SM10 heat) and test environments (air in this work versus ~10^{-6} torr vacuum of the SM10 heat). The tearing modulus of the FCRD-NFA1 heat had a relatively constant value of ~6.6±2.1 at 25–600°C, which quickly increased to 36.5 at 700°C. This phenomenon in temperature-dependent tearing modulus was also observed in Grade 91.

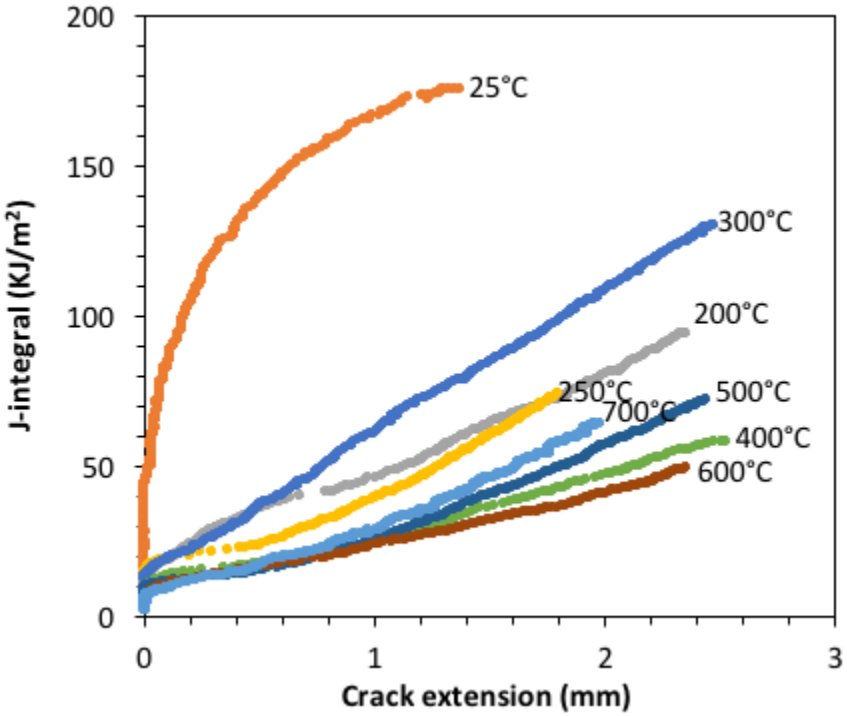

Figure 10. J-R curves of 14YWT tested at 25 to 700°C.

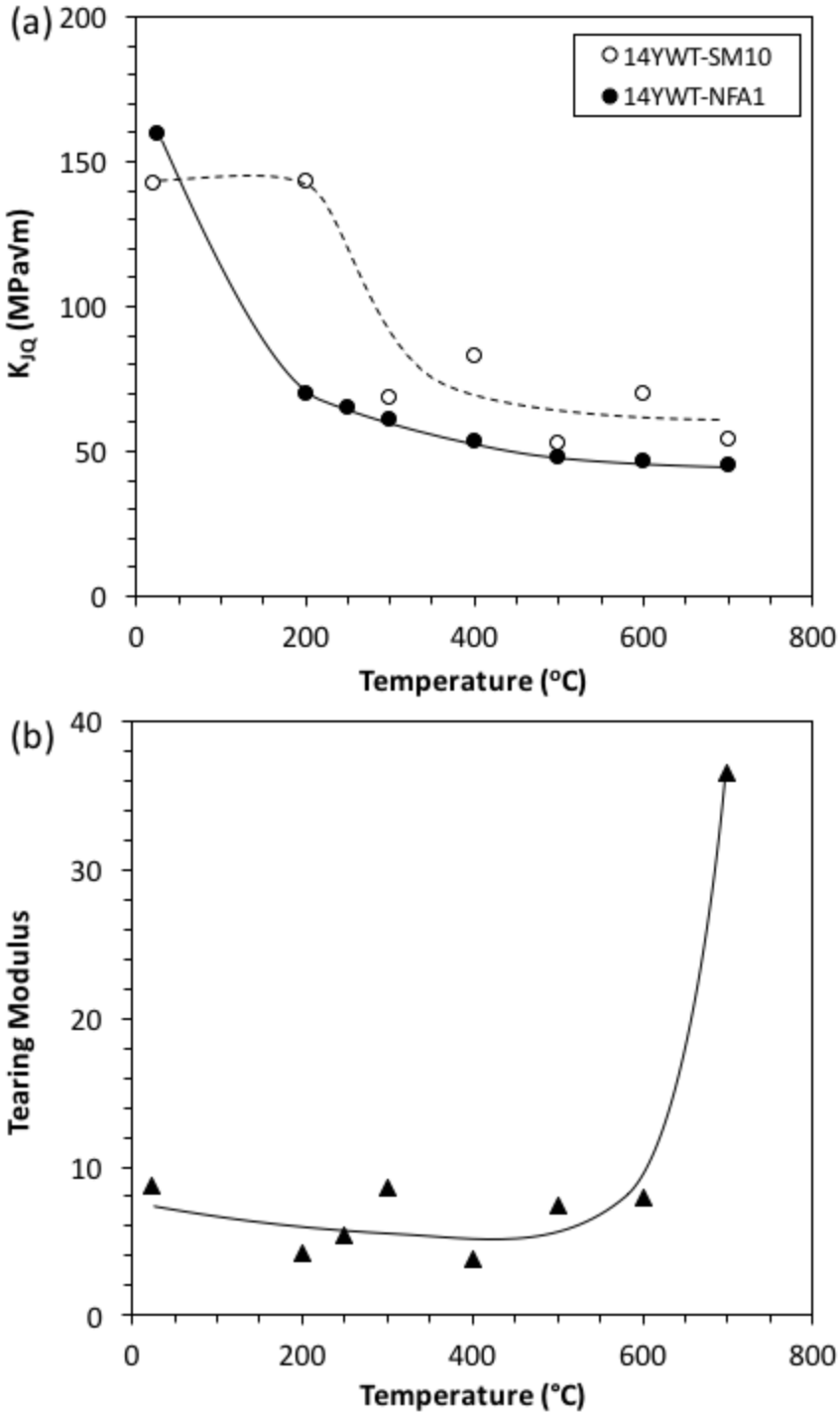

Figure 11. Fracture toughness and tearing modulus of 14YWT in the ductile regime at 25–700°C.

3. HIGH-TEMPERATURE STEAM OXIDATION

Coupons in a size of 1.5 × 10 × 19 mm were extracted from the procured alloys for high-temperature steam oxidation tests. The coupons were polished to a 600 grit SiC finish and cleaned ultrasonically in acetone and methanol. Tube furnaces, as shown in Figure 12, were customized for tests at 1 atmosphere with full steam containing ~10 part-per-billion (ppb) oxygen content. Five coupons per alloy have been tested at 600 and 650°C, respectively, with a targeted exposure time of 5000 h. The coupons were weighted prior to the exposure and after every 500-h exposure using a Mettler-Toledo model XP205 balance with an accuracy of 0.04 mg or 0.01 mg/cm^2. Optical microscopy was employed to characterize the surface morphology and cross-section oxide scales of the exposed coupons.

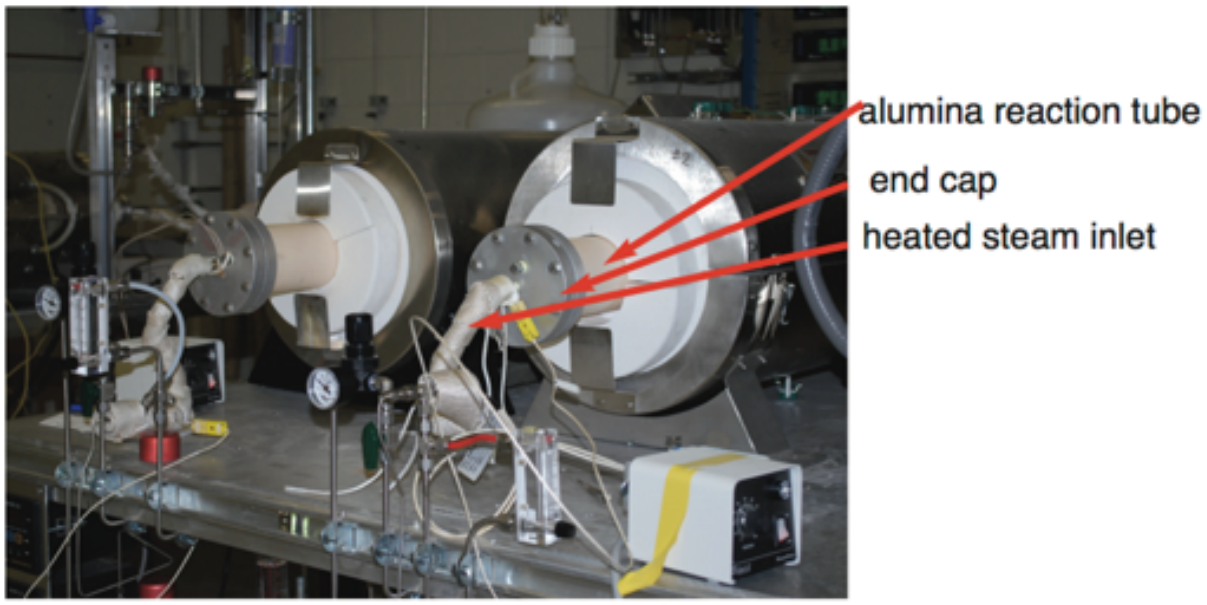

Figure 12. High-temperature steam oxidation test facility.

Figure 13 shows 500-h exposed coupons of some alloys at 600 and 650°C, which were arranged in the crucibles during the exposures. Different colors formed on the coupons due to the specific forms of oxides formed on the alloys. The exposed Zr–2.5Nb coupons showed the most distinctive feature as shown for the five coupons at the upper-right corner of Figure 13. Photos of the Zr–2.5Nb coupons at a higher magnification in Figure 14 exhibit grainy oxide scales with thick fuzzy oxides at edges after exposure at 600°C, which became severer at 650°C. Steam oxidation test of Zr–2.5Nb coupons was not continued after the 500-h exposure because of their aggressive oxidation behavior, resulting in exceptional weight gains as shown in Figure 15.

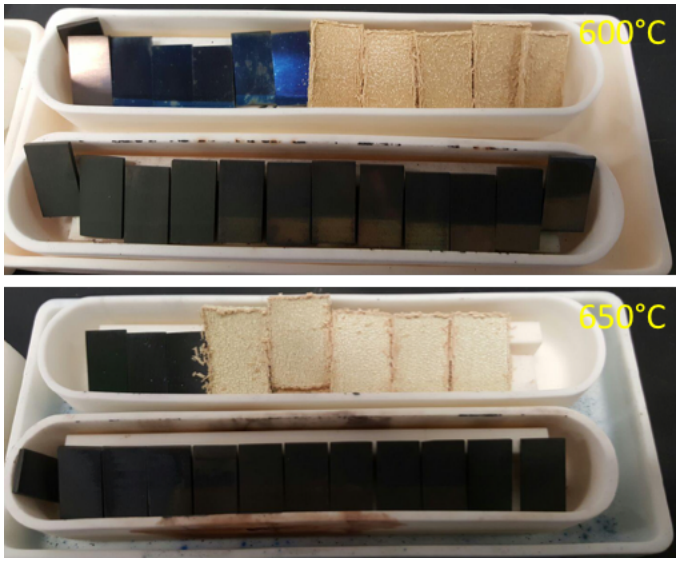

Figure 13. Photos of the tested alloy coupons in crucibles exposed to steam at 600 and 650°C for 500 h.

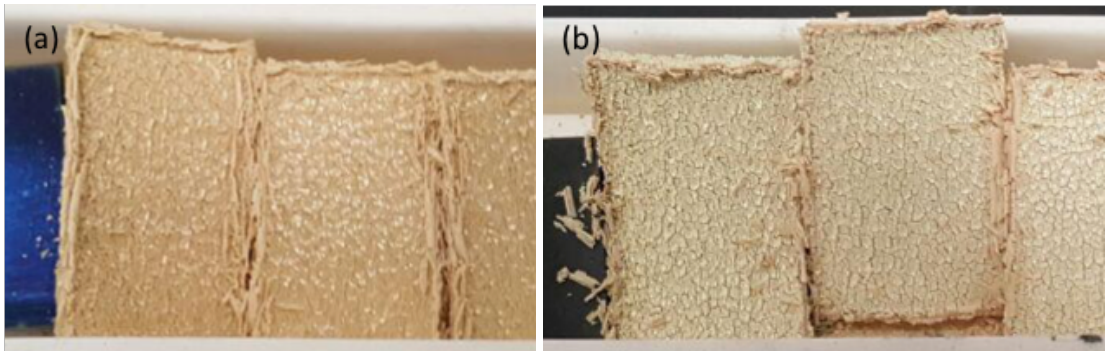

Figure 14. Photos of the 500-h exposed Zr–2.5Nb coupons at (a) 600 and (b) 650°C.

Weight changes of the exposed coupons of Zr–2.5Nb, 316L, 706, and ferritic steels (i.e., Grade 92, Alloy 439, and 14YWT) are plotted in Figure 15. Alloy 706 [heat 011509] was tested because it was considered to be Alloy 310 when received from Carpenter Technology. The untested alloys, such as 310, 718, X750, and Grade 26 Ti-alloy, will be tested when the alloy coupons are available. Exposure of five coupons per alloy was initiated at the same time, with one coupon taken out of the tests for potential microstructural characterization after 500, 1000, and 2000 h exposures, leaving two coupons exposure to 5000 h. The symbols on each line track the weight changes every 500-h exposure for the same coupon. Alloy 706 showed negligible weight gains compared to the other alloys at both test temperatures. Alloy Zr–2.5Nb showed >20 and >~50 mg/cm^2 weight gains after 500-h exposure at 600 and 650°C, respectively, which are about twice of the weight gains of Grade 92. The exceptional weight gains of Zr–2.5Nb are caused by the extensive oxidation as shown in Figure 14. The three ferritic steels showed noticeably weight gains, with Grade 92, Alloy 439, and 14YWT in a descending order. The weight gains of Grade 92 at 650°C were about twice of that at 600°C. In contrast, Alloy 439 did not show much difference in weight gains at the two temperatures, which may be attributable to its high chromium content (18Cr). Interestingly, 14YWT exhibited weight gains at 650°C, which are less than half of that at 600°C. It may be attributable to the ultrafine grains (~0.8 μm) of 14YWT. In contrast to the weight gains of Zr–2.5Nb and the ferritic steels, austenitic stainless steel 316L exhibited significant weight losses, which get severer at 650°C.

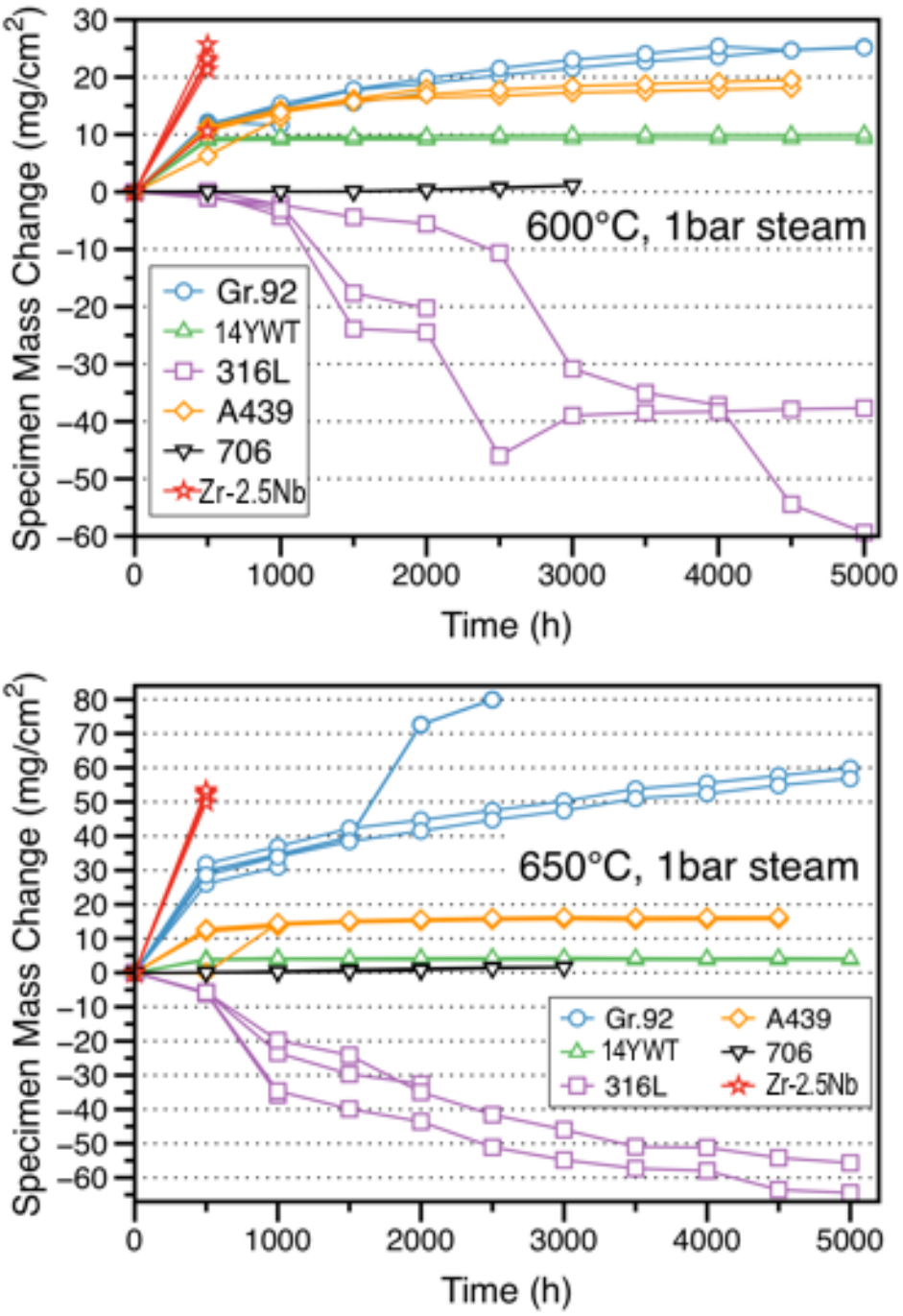

Figure 15. Weight changes of Zr–2.5Nb, 316L, 706, and ferritic steels exposed at (a) 600 and (b) 650°C.

Similarly, Figure 16 shows the weight changes of the exposed coupons of Alloy 800 and Ni-based superalloys (i.e., 625, 625 directly aged, 625-plus, 690, 706, 725, and C22). Alloy 800 and the Ni-based superalloys showed very low weight gains compared to the ferritic steels in Figure 15. Comparable weight gains were observed for Alloys 800 and 706 at 600°C. The weight gains of Alloy 706 tend to be slightly higher than Alloy 800 at 600°C. Alloy C22 exhibited slight weight losses at 600°C. In general,

Alloy 625, 625DA, 625-plus, 690, and 725, showed negligible weight changes at 600°C, which had slight weight gains during short time exposures and then changed to slight weight losses. In comparison, the 650°C exposure tests resulted in relatively stable or protective oxide growth with different weight gains. Not necessarily following the order in weight changes at 600°C, Alloy 725 showed the greatest weight gains, followed by 625-plus, 800, C22, 690, 625DA, and 625 in an approximately descending order that is not able to be well differentiated.

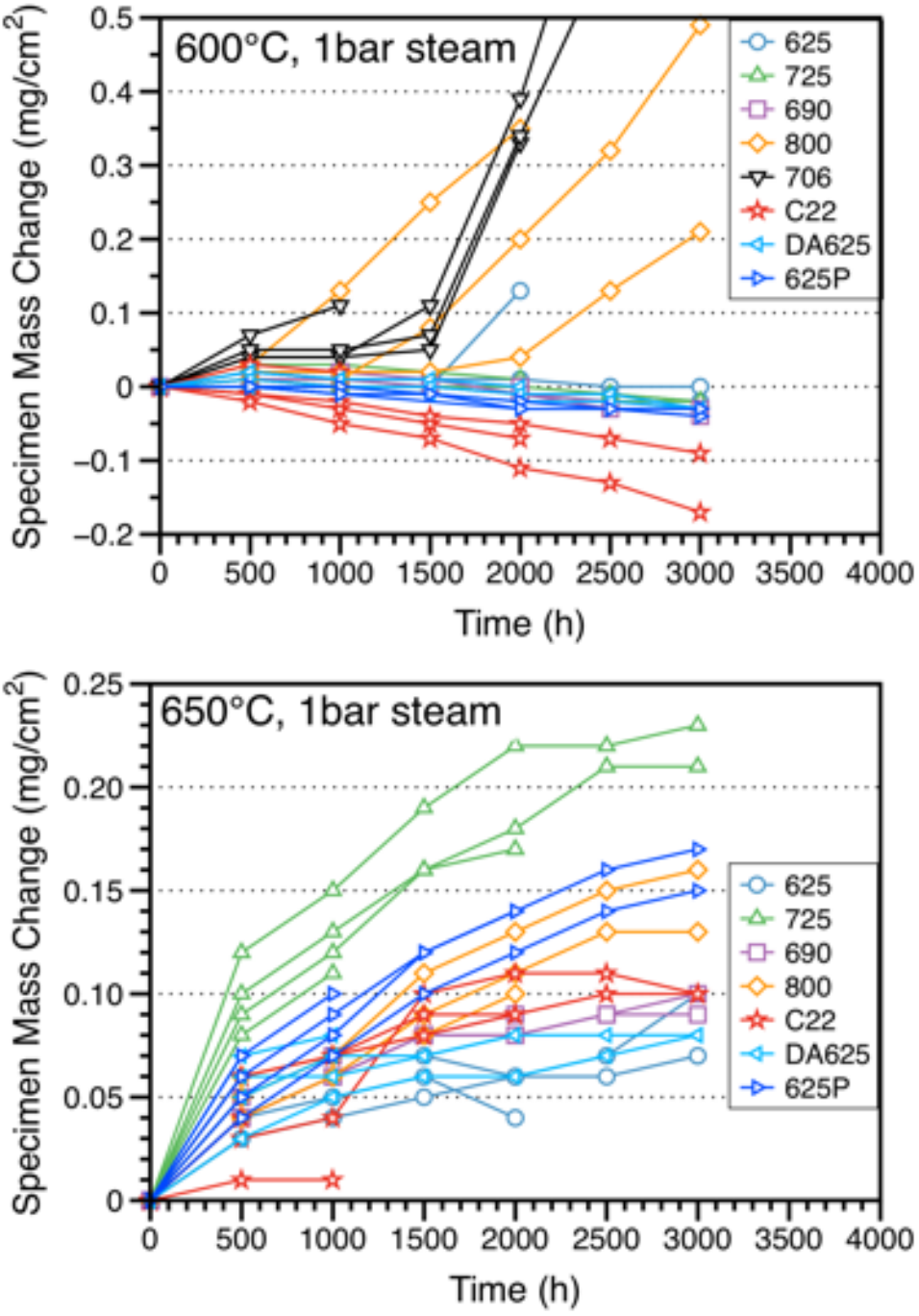

Figure 16. Weight changes of Alloy 800 and Ni-based superalloys exposed at (a) 600 and (b) 650°C.

Figure 17 shows the typical surface morphologies of the coupons of 316L, Grade 92, Alloy 439, and 14YWT exposed at 600 and 650°C for 1000 h. In contrast to scale exfoliation at some areas at 600°C, nearly all the scales were exfoliated on the 316L at 650°C, which are consistent with their significant weight losses. Some scale exfoliation was also observed on Grade 92 at both 600 and 650°C, but not much on Alloy 439 and 14YWT.

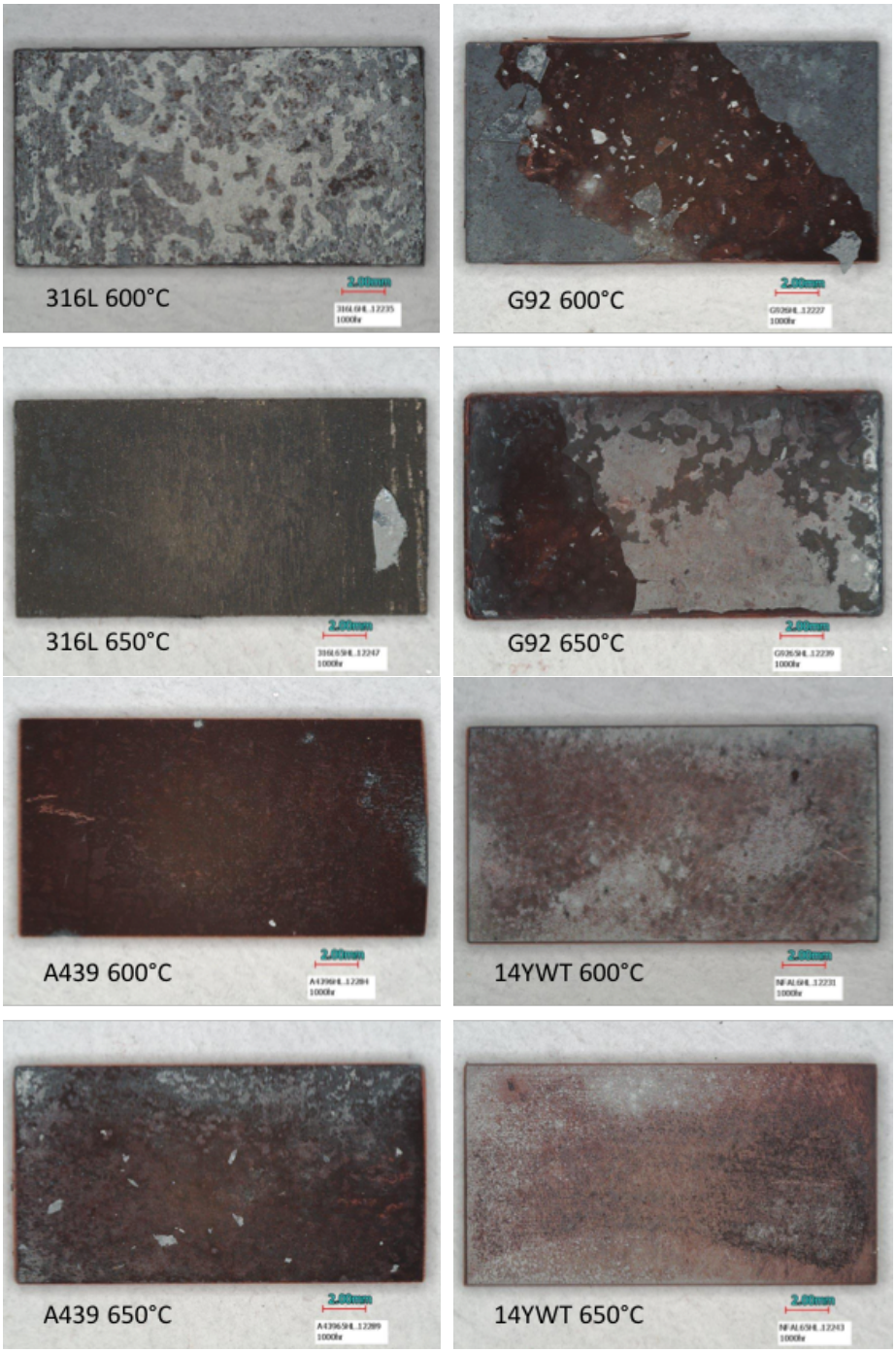

Figure 17. Optical images of the surface morphologies of the 1000-h exposed coupons of 316L, G92, A439, and 14YWT at 600 and 650°C.

Cross-sectional specimens of the 1000-h exposed coupons of 316L, Grade 92, Alloy 439, and 14YWT were prepared to characterize the structure of their oxide scales. Figure 18 shows the typical images, taken from the locations with relatively well-retained oxide scales. The oxide scale formed on 316L at 600°C is approximately composed of four layers, with cracks primarily observed at the interface of the two outer layers. In contrast, only a semi-continuous thin layer of scale was observed on 316L at 650°C, which may be corresponding to the innermost discontinuous diffusion layer on 316L at 600°C.

The oxide scale on Grade 92 is primarily composed of two layers at 600°C. Exposure of Grade 92 at 650°C resulted in significant growth of the two layers, together with the formation of an additional diffusion layer at the metal-scale interface and another thin layer at surface. The higher temperature exposure also significantly increased the amount of pores or cracks at the outer-inner-scale interface. A three-layer scale structure formed on Alloy 439 at 600°C, which become primarily a two-layer scale structure at 650°C. The scale thickness on Alloy 439 at 650°C (~117 μm) is >2.2 times of that at 600°C (~51 μm), which is different from the similar weight gains as shown in Figure 15. Detailed microstructural analysis of the oxide scales is needed to understand the discrepancy. The four-layer oxide structure on 14YWT at 600°C is somewhat similar to that on Grade 92 at 650°C, except for the significantly thinner oxide scale and the cracks in the outer layer. The 650°C exposure of 14YWT resulted in a two-layer oxide structure similar to the oxide scale on Grade 92 at 600°C. It's interesting to find that the oxide scale thickness on 14YWT at 600°C (~126 μm) is similar to that on Alloy 439 at 650°C, but the scale thickness on 14YWT at 650°C (~42 μm) is about the same as that on Alloy 439 at 600°C. The scale thickness on 14YWT at 650°C is about 1/3 of that at 600°C, which is approximately consistent with the relationship of the measured weight gains in Figure 15. Detailed analysis is needed to understand the changes in oxidation mechanisms at the two temperatures.

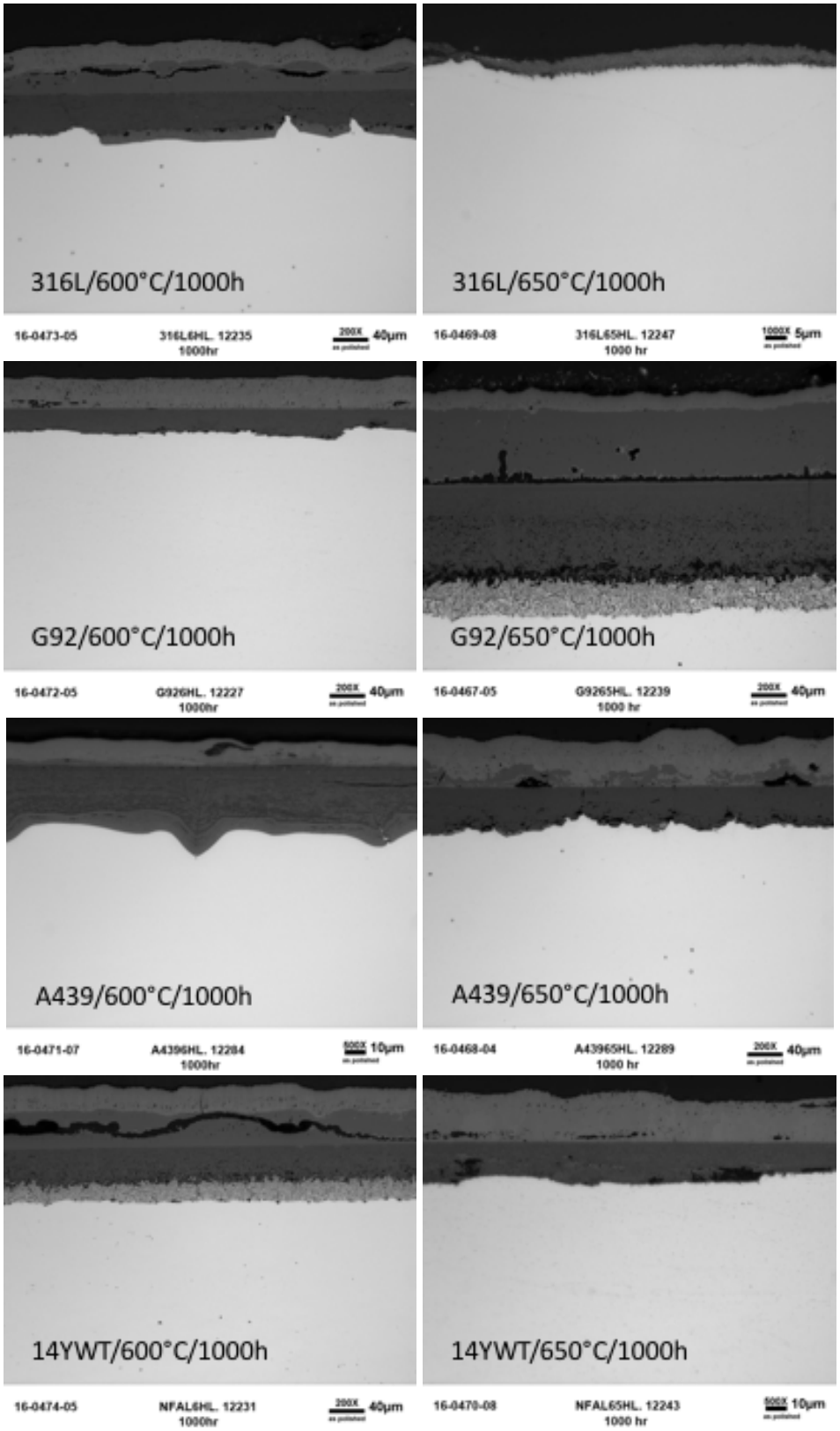

Figure 18. Optical images of the cross-section oxide scales formed on the 1000-h exposed coupons of 316L, G92, A439, and 14YWT at 600 and 650°C.

4. SUMMARY

A total of fifteen commercial and advanced alloys (including three variants of Alloy 625) have been down-selected for investigation under the ARRM program. Thirteen of the alloys, together with 316L and T91 as the reference steels, have been procured. It includes a total of one zirconium alloy (Zr–2.5Nb), four ferritic steels (T91, Grade 92, Alloy 439, and 14YWT), three austenitic stainless steels (316L, 310, and 800), and eight Ni-based superalloys (625, 625DA, 625-plus, 690, 725, X750, and C22). The procurement of the other down-selected alloys such as 718 and Grade 26 Ti-alloy is in progress.

Most of the procured alloys have acceptable microstructures for tests under the ARRM program. However, the as-procured Alloy 439 is not acceptable because of the coarse grains and presence of many intragranular cracks. A TMT was successfully developed on the as-procured Alloy 439, achieving significantly refined grains. To have acceptable "flawless" microstructure for mechanical property and ion irradiation resistance screening, ultrasonic NDE was used to guide specimen extraction. The fine-grained Alloy 439 exhibited some increases in both strength and ductility, as well as improvements in Charpy impact toughness, compared to the as-procured coarse-grained Alloy 439. 14YWT showed significantly greater strength than Grade 92 and Alloy 439, with ductility comparable to Grade 92 but less than Alloy 439. Alloy 439 exhibited the highest USE (~57 J) with a mathematical DBTT of 16.0°C at 1/2USE in the T–L orientation, which are higher than Grade 92 with an USE of ~27 J and a DBTT of −19.7°C. The super-high strength of 14YWT led to a low USE of ~5 J with a low mathematical DBTT of −79.8°C. A quick decrease in fracture toughness from ~160 MPa√m at room temperature to ≤69 MPa√m at temperatures above 200°C, accompanied with a quick increase in tearing modulus from ~6.6±2.1 at 25–600°C to 36.5 at 700°C, was observed in the tests of 14YWT in the ductile regime.

Steam oxidation tests at 1 atmosphere with ~10 ppb oxygen at 600 and 650°C were conducted on the procured alloy coupons, which were weighed at 500-h intervals with a targeted exposure time of 5000 h. Alloy Zr–2.5Nb was only tested one cycle (500 h) at 600 and 650°C because of the exceptional weight gains and extensive oxide scales formed on the coupons. Ferric steels Grade 92, Alloy 439, and 14YWT showed moderate weight gains in a descending order, which are believed to be primarily determined by the chromium content (9, 18, and 14Cr, respectively) and grain size (~40, ~50, and ~0.8 μm, respectively) in the steels. Oxide scale characterization by optical microscopy revealed approximate consistency between the scale thickness and weight gains of Grade 92 and 14YWT, but not Alloy 439. Detailed analysis will be conducted. Austenitic stainless steel 316L exhibited significant weight losses with extensive scale exfoliation. The significantly increased amounts of chromium and nickel in Alloy 800 and the Ni-based superalloys led to small or negligible weight changes. Detailed ranking regarding the steam oxidation resistance of the alloy will be deduced when all the alloy coupons accomplish 5000 h exposures at 600 and 650°C in next fiscal year.

In summary, this year's research and development activities primarily included four aspects: procured Alloy X-750 from Carpenter Technology and Bodycote; refined the grain size of the as-procured Alloy 439 to complete Charpy V-notch impact tests of ferritic steels; completed fracture toughness at ductile regime of 14YWT; and initiated and partially completed steam oxidation tests of the procured alloys.

REFERENCES

[1] E.A. Kenik, J.T. Busby, Radiation-induced degradation of stainless steel light water reactor internals, Mater. Sci. Eng. R 73 (2012) 67–83.

[2] F.A. Garner, Radiation damage in austenitic steels, in: R.J.M. Konings, T.R. Allen, R.E. Stoller, S. Yamanaka, Comprehensive Nuclear Materials, Elsevier, The Netherlands, 2012.

[3] L. Tan, R.E. Stoller, K.G. Field, Y. Yang, H. Nam, D. Morgan, B.D. Wirth, M.N. Gussev, J.T. Busby, Microstructural evolution of type 304 and 316 stainless steels under neutron irradiation at LWR relevant conditions, JOM 68 (2016) 517–529.

[4] Critical Issues Report and Roadmap for the Advanced Radiation-Resistant Materials Program, EPRI, Palo Alto, CA and the U.S. Department of Energy, Washington, DC: 2012. 1026482.

[5] L. Tan, M.A. Sokolov, D.T. Hoelzer, J.T. Busby, Tensile and toughness assessment of the procured advanced alloys, ORNL/TM-2015/469, September 11, 2015.

[6] M.A. Sokolov, R.K. Nanstad, On impact testing of subsize Charpy V-notch type specimens, in: D.S. Gelles, R.K. Nanstad, A.S. Kumar, E.A. Little (Eds.), Effects of Radiation on Materials: 17th International Symposium, ASTM STP 1270, 1996, pp. 384.

[7] T.S. Byun, J.H. Kim, J.H. Yoon, D.T. Hoelzer, High temperature fracture characteristics of a nanostructured ferritic alloy (NFA), J. Nucl. Mater. 407 (2010) 78–82.